Materials Characterization 145 (2018) 1–9

Contents lists available at ScienceDirect

Materials Characterization

journal homepage: www.elsevier.com/locate/matchar

Generation and healing of porosity in high purity copper by high-pressure torsion

Yuanshen Qi[a,*], Anna Kosinova[a], Askar R. Kilmametov[b], Boris B. Straumal[b,c,d], Eugen Rabkin[a,*]

[a] Department of Materials Science and Engineering, Technion – Israel Institute of Technology, 32000 Haifa, Israel
[b] Karlsruhe Institute of Technology, Institute of Nanotechnology, Eggenstein-Leopoldshafen, Germany
[c] National University of Science and Technology «MISIS», Moscow, Russia
[d] Institute of Solid State Physics, Russian Academy of Sciences, Chernogolovka, Russia

ARTICLE INFO

Keywords:
High-pressure torsion
Severe plastic deformation
Porosity
Copper
Vacancy
Diffusion

ABSTRACT

Generation and healing of pores in metals under loading or during processing have long been important research topics, and their mechanisms are still debatable. In recent years, unexpected percolating networks of pores acting as ultra-fast diffusion paths were found in ultrafine-grained metals processed by severe plastic deformation. Herein, we conducted a systematic study of the mechanisms of generation and healing of pores in ultrahigh-purity copper (99.9995 wt%) during high-pressure torsion (HPT). In addition to a solid Cu disk, the disk with holes that were drilled before processing, resulting in nominal initial porosity of 4.48%, was processed by HPT. After HPT, the percolating porosities of 0.07 ± 0.01% and 0.04 ± 0.01% were found in the solid disk, and in the disk with pre-fabricated holes, respectively. Thus, higher initial porosity resulted in lower percolating porosity in the HPT-processed disk. Systemic characterization using scanning electron microscopy revealed that in both cases shear bands and ultra-fine grains are located in the regions with induced and healed pores. We discussed the mechanisms of porosity evolution in both cases. In the end, to verify the possibility of pores nucleation and growth by vacancy agglomeration, vacancy diffusivity during HPT processing was estimated. This work sheds a new light on the mechanisms of pores nucleation and evolution during severe plastic deformation.

1. Introduction

Generation and healing of pores in metals under loading or during processing have long been important research topics in physical and mechanical metallurgy. Evolution of pores or voids in bulk metallic materials has been extensively studied for better control of the ductile failure during plastic deformation [1]. It has been generally accepted that the generation of voids and their growth and coalescence are caused by high stress triaxiality under hydrostatic tension, i.e. the high value of the ratio of the mean stress to the equivalent stress [2,3]. On the contrary, hydrostatic pressure is essential for elimination of pre-existing voids. Studies have shown that porosity in as-cast metallic materials resulting from solidification can be eliminated by metalworking processes such as forging, rolling, etc. [4,5]. Evolution and healing of pre-existing porosity under plastic deformation has been studied using metal samples with artificially drilled holes [6]. It was found that hydrostatic pressure and shear strain enhance the collapse and closure of pores and formation of sound bonding of the internal surfaces after they are brought into intimate atomic contact [6–9].

Hydrostatic pressure and shear strain are two indispensable features in most severe plastic deformation (SPD) techniques for producing ultrafine-grained metallic materials [10,11]. Moreover, the combination of ultrahigh hydrostatic pressure and simple shear allows consolidation of particulate materials to nearly full densification by eliminating porosity and building strong inter-particulate metallic bonding [12,13]. However, recent studies revealed that unexpected percolating porosity - a network of interconnected internal cavities, can be induced in bulk solid metallic samples during SPD processing, such as equal-channel angular pressing (ECAP) and high-pressure torsion (HPT) [14–19]. This is surprizing, since a combination of high hydrostatic pressure and shear deformation imposed by SPD should supposedly lead to reduction of porosity. Therefore, one can conclude that the SPD processing may lead to two opposite impacts on the porosity evolution, i.e. simultaneous generation and healing of pores.

* Corresponding authors.
E-mail addresses: yuanshen.qi@technion.ac.il (Y. Qi), anna.kosinova@technion.ac.il (A. Kosinova), askar.kilmametov@kit.edu (A.R. Kilmametov), straumal@issp.ac.ru (B.B. Straumal), erabkin@technion.ac.il (E. Rabkin).

https://doi.org/10.1016/j.matchar.2018.08.023
Received 10 April 2018; Received in revised form 3 August 2018; Accepted 13 August 2018
Available online 15 August 2018

The percolating porosity induced by SPD was previously uncovered and quantified using radiotracer diffusion measurements [14,15]. Direct characterization of the pores in pure materials, regarding to their specific locations, morphologies and their effects on surrounding microstructures has not been systematically conducted. In addition, to the best knowledge of the authors, the efficiency of HPT in healing of pre-existing porosity has never been addressed.

To study both generation and healing of porosity during HPT process, two ultra-high purity copper disks, one in its bulk form and the other one with artificially drilled holes for introducing a pre-existing porosity were processed and characterized. Using electron microscopy characterization, the mechanisms of porosity generation and healing are analyzed. In the end, porosity formation is discussed in terms of accelerated vacancy diffusion during HPT.

2. Materials and Methods

Two high purity (99.9995 wt% or 5N5) Cu disks were processed by HPT at room temperature. One Cu disk of 10 mm in diameter and 0.7 mm in thickness was solid (in what follows "Cu disk"), while the other Cu disk of the same purity and dimensions had seven cylindrical holes of 0.8 mm in diameter drilled through the thickness (in what follows, "Cu-Holes disk"). One hole was located at the center and other six were located about 2.5 mm away from the center and 60° away from each other. Seven holes resulted in a porosity of 4.48%. The schematic illustration of the material and processing scheme is shown in Fig. 1. The HPT processing (5 anvil rotations at a rotation rate of 1 revolution per minute) was carried out under compressive pressure of 5 GPa in a Bridgman anvil-type unit with a quasi-constrained die using a custom-built computer controlled HPT device (W. Klement GmbH, Lang, Austria). After processing, the thickness of the disks decreased from 0.7 mm to ~0.4 mm and the diameter expanded from 10 mm to ~12 mm.

The microstructure characterization was conducted on the cross-section area of the disks. In what follows we assigned the labels normal direction (ND), shearing direction (SD), and transverse direction (TD) to the disk normal, to the in-plane direction in the cross-section orthogonal to ND, and to the out-of-cross-section direction, respectively (see Fig. 1). It should be noted, however, that the true shearing and transverse directions (SD′ and TD′) are the tangential and radial directions which change with respect to the location of the characterized regions. After processing, the disk was cut 3 mm away from its center and conventional sandwich specimens were made by gluing two Cu plates with similar sizes on each side of the sample, see Fig. 1. It is worth noting that after HPT 5 rotations under the pressure of 5 GPa, the microstructure of Cu samples of conventional purity should be homogeneous throughout the sample, both in radial and axial directions [20]. Epoxy was used to glue the two halves together and the curing was conducted on a hot plate at 120 °C for 20 min. Conventional grinding using SiC paper down to 4000 grit and final mechanical polishing using 50 nm Al_2O_3 suspension were conducted. Final electropolishing was carried out at room temperature in 14 M phosphoric acid by applying electric potential of 1.2 V. Time of about 2 min was sufficient to remove the damaged surface layer and reveal the grains. After electropolishing the samples were rinsed with distilled water. High resolution scanning electron microscopy (HRSEM) and electron backscattered diffraction (EBSD) measurements were carried out using a Zeiss Ultra Plus SEM equipped with a Bruker EBSD detector. Three SEM imaging detectors were used to collect images for obtaining different information, namely a conventional secondary electron (SE) detector, an in-lens secondary electron detector, and a backscattered electron (BSE) detector. SEM in-lens images exhibit lower topographic and atomic number contrasts, but allow identification of pores with a better resolution than SEM-SE and BSE images [21]. Therefore, the volume fraction of pores was calculated based on the images acquired using in-lens detector. Focused ion beam (FIB) regular cross-section milling was carried out using a FEI Helios NanoLab DualBeam G3. For calculation of average grain size, twins and subgrains defined by the low-angle grain boundaries (LAGBs) with misorientation angle below 15° were not accounted for as individual grains. Moreover, average grain size was calculated based on area weight fraction, instead of number fraction.

3. Results

We characterized the distribution, morphologies, arrangement, and volume fractions of the pores in the as-cast material, in the HPT-processed Cu disk as well in the Cu-Holes disk. We also determined the grain size distribution and crystallographic orientations of the grains, paying special attention to the regions in the vicinity of induced pores and pre-existing holes.

3.1. Porosity Evolution

The grain boundaries (GBs) in the as-cast Cu sample (with the average grain size around 300 μm, see Ref. [22]) are decorated with small pores, as shown in Fig. 2(a, b). These pores have an average size of 3.52 ± 1.49 μm and make up 0.07 ± 0.01 vol% in the cross-section area. The volume fraction of the pore areas was determined by segmentation using ImageJ software. The threshold value was adjusted carefully in each image to ensure accuracy and the uncertainty in each measurement was about 0.01%. One representative segmented image is shown in Fig. 2(c). The formation of pores due to vacancy annihilation at the GBs during solidification is well-documented [23]. The micrometer dimensions of the pores are probably related to the high mobility of the vacancies owing to the extremely low impurity level. At melting temperature, the vacancy concentration is around 10^{-4}, which exceeds by at least factor of 20 the concentration of impurities in the studied

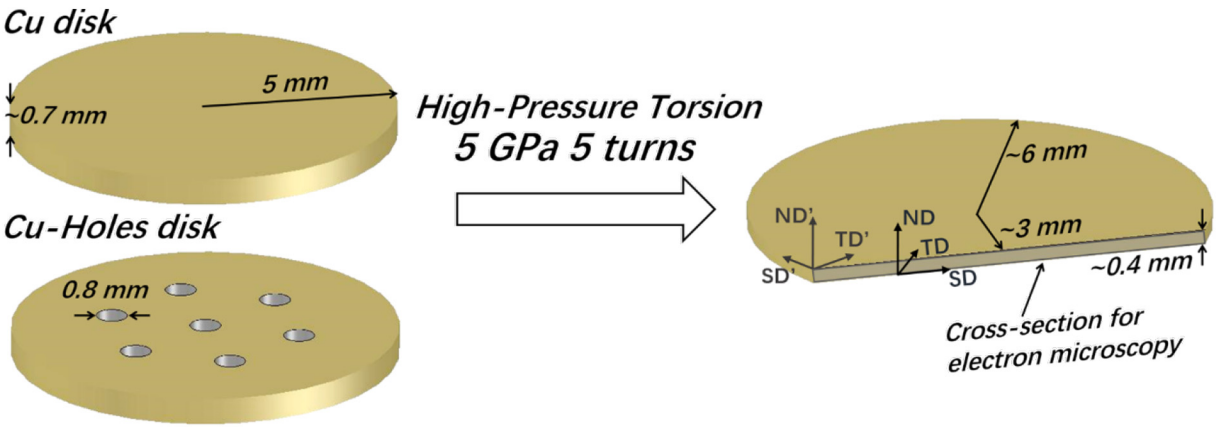

Fig. 1. Schematic illustration of the specimens and processing route. Note the difference between the coordinate systems (ND, SD, TD) and (ND′, SD′, TD′).

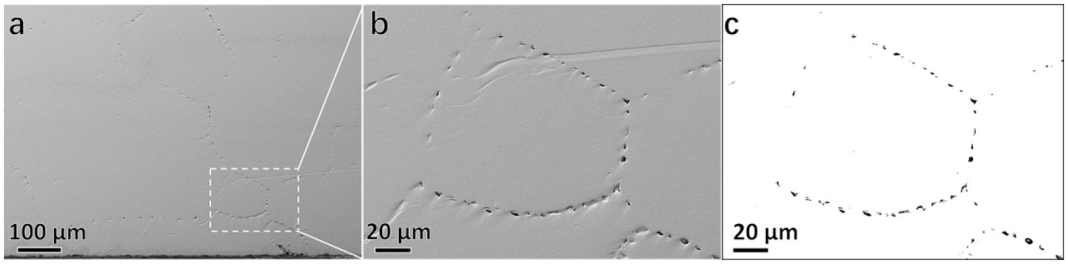

Fig. 2. The SEM-SE image (a) showing the cross-section of the Cu disk cut from as-cast material, (b) pores located at the GBs were pointed out and (c) the segmentation of the voids is demonstrated.

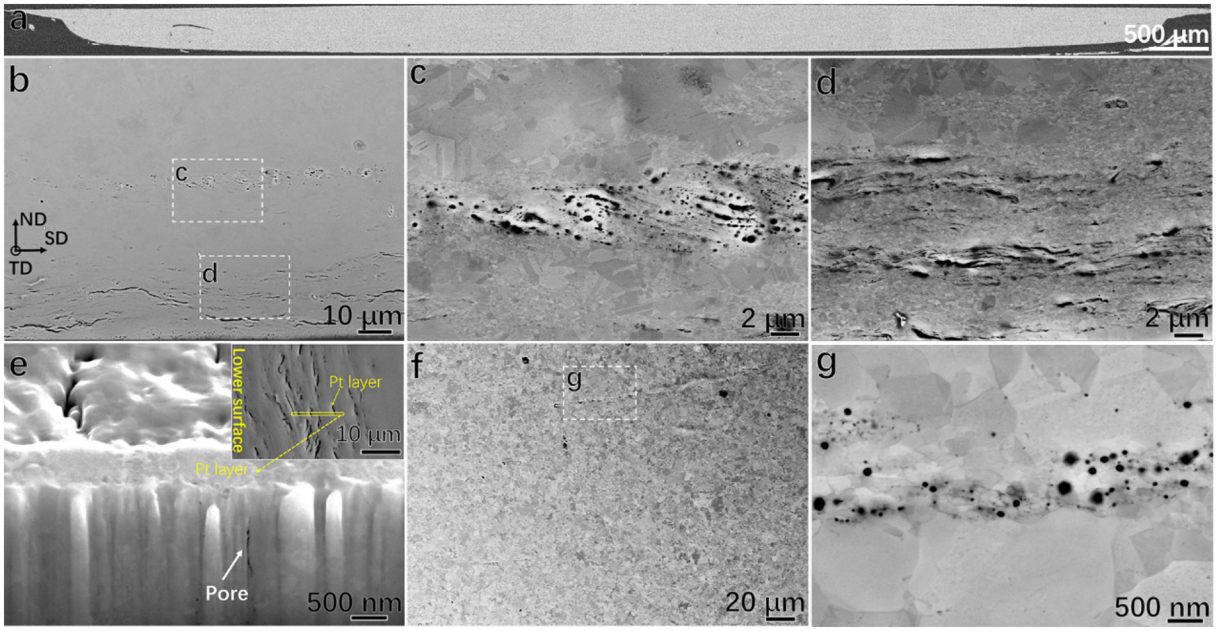

Fig. 3. SEM-SE image (a) showing the overall cross-section view of the HPT-processed Cu disk, SEM-SE image (b) and SEM-BSE images (c, d) showing the formation of porosity and ultrafine grain clusters near the bottom surface, BSE image (e) showing the cross-section view of the pores by FIB milling, insert demonstrates where the trench was cut, BSE images (f, g) showing few porosities and micro-sized grains in the central area. Dashed boxes in (b, f) showing the locations of (c, d, and g).

material.

The overall view of the cross-section of the Cu disk after HPT is shown in Fig. 3(a). The lateral out-flow of the material at the upper surface is clearly seen. The porosity of 0.07 ± 0.01% was determined by checking the whole cross-section area using high magnification SEM images. Approximately 78% and 16% of pores were generated within 50 μm from the lower and upper external surface, respectively. This is consistent with the results of radiotracer diffusion measurement in the ECAP processed Cu, where the ultrafast diffusion paths penetrated to the depth of about 30 μm from the surface [24,25]. Apart from the regions near external surfaces, the central area in the cross-section exhibited only insignificant porosity (the remaining 6% of all pores). This means that HPT induced porosities were not homogeneously distributed through the thickness of the disk. This difference was a direct result of heterogeneous plastic flow which could be affected by various processing parameters such as disk thickness, die geometry, friction condition between anvils and disk, applied pressure, strain rate, and misalignment of the axes of anvils [26–32].

In Fig. 3(b), the porosities near the lower external surface are classified into two groups with respect to their locations and morphologies, and presented with higher magnification in Fig. 3(c, d). The Fig. 3(c) shows the pores formed at a distance of about 50 μm from the bottom surface, which are arranged in the form of a band 3–5 μm wide and longer than 100 μm. The pores within the band have nearly rounded shape with low aspect ratio, c.f. 0.17 ± 0.05 μm in normal direction (ND) and 0.24 ± 0.11 μm in shearing direction (SD). The Fig. 3(d) shows pores formed close to the bottom surface, which are arranged in the form of a band of about 20 μm in width. Their average lengths along the ND and SD are 0.22 ± 0.09 μm and 2.46 ± 1.97 μm, respectively. These elongated pores could be formed by growth of the single pores and/or their coalescence, and the band could be formed by shear band slip movement. One important feature shared by these two regions is the co-existence of ultrafine grains (UFGs) with the pores within the bands. To check the length of the pores in transversal direction (TD), a trench was cut using FIB, and the corresponding SEM image is shown in Fig. 3(e). One pore was found propagating parallel to the external surface with a length of 0.67 μm in TD. This observation is similar to the pores found in the work of Ribbe et al. and again proves the existence of the network of porosity [14].

The microstructure in the central region (Fig. 3f) is more homogenous and has a lower porosity than the one close to external surfaces. In an enlarged view in Fig. 3(g), it can be seen that the pores have rounded shape and smaller dimensions, with average lengths of 0.07 ± 0.03 μm and 0.08 ± 0.03 μm in ND and SD, respectively. In contrast to the region near external surfaces, no extensive grain refinement and shear band was found around these pores. Therefore, they were supposed to be induced during unloading/recovery stage and caused by vacancy agglomeration along grain boundaries or triple junctions [15]. Indeed, Schafler's study showed that in the unloading stage, the vacancy concentration dropped to half of the value achieved

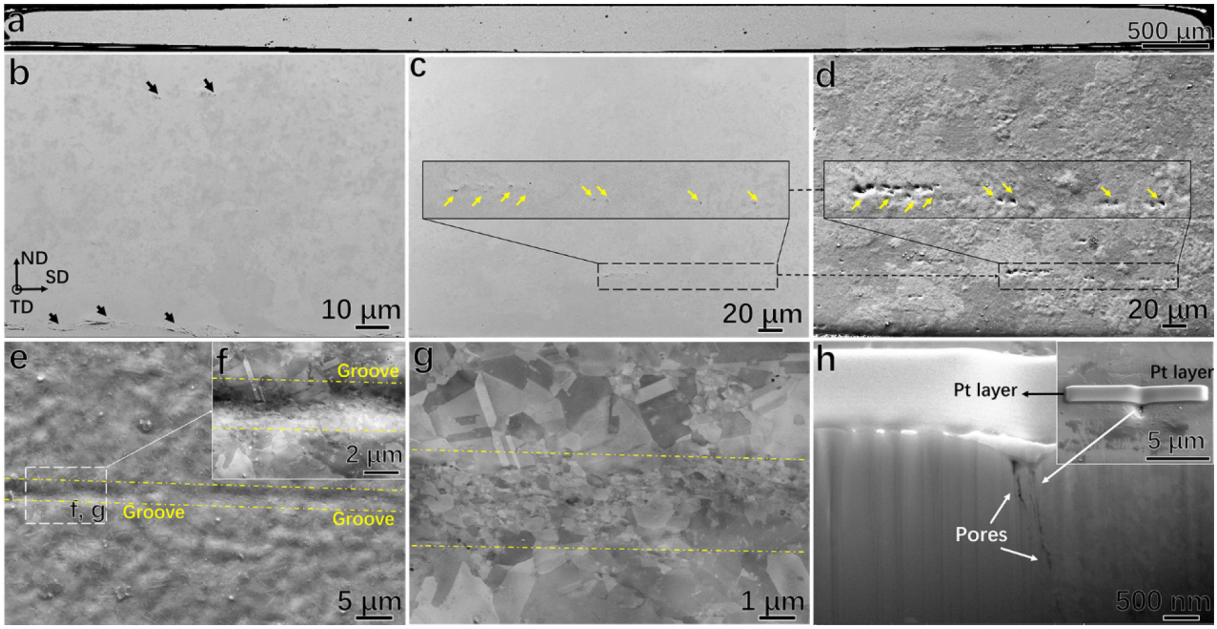

Fig. 4. SEM-SE image (a) showing the overall cross-section view of the HPT-processed Cu-Holes disk, (b) showing the pores, (c, d) demonstrating the comparison between the information collected by in-lens and SE detectors for porosity imaging, SE image (e, f) showing the topography features used for distinguishing grooves, SEM-BSE image (g) showing the same area as (f) to highlight the ultrafine grains in a groove, BSE image (h) showing the cross-section view of the pores prepared by FIB milling, insert demonstrates where the trench was cut.

during HPT [33]. This amount of vacancies could agglomerate into voids. In summary, the pores found near the external surfaces had high aspect ratios and co-existed with UFG clusters, while the ones in the central regions had nearly rounded shape and were not associated with the regions of refined grains.

From the cross-section view of the HPT-processed Cu-Holes disk in Fig. 4(a), no micrometer-sized residual pores were found, indicating the pre-existing porosities – seven 0.8 mm diameter holes – were closed up during the processing. In fact, the porosity decreased dramatically from 4.48% to 0.04 ± 0.01% after the HPT process, based on the calculation using high resolution SEM images. In addition to the diminishment of the holes, another outstanding feature is that no significant lateral outflow of material was observed. This means that due to the existence of the pre-existing internal pores, materials tended to flow inwards to close the holes during HPT, rather than outwards. With closer observation in Fig. 4(b), most of the area is free of any pores. The pores in the vicinity of the external surface have similar morphologies to the ones in Fig. 3(b), but are fewer in number and are concentrated in a narrower band than their counterparts in the Cu disk. Therefore, the HPT process healed the disk with holes by eliminating the internal surfaces.

To find the healed regions of the pre-existing holes, we employed the SEM imaging in the SE mode. Fig. 4(c–f) demonstrate that SE images are suitable for tracking the healed areas of pre-existing holes (pointed by yellow arrows) by distinguishing the grooves from the matrix, but at the same time they exaggerate the size of the true pores. The grooves shown in Fig. 4(e, f) as topography features were introduced by electro-polishing and they can only originate from the healed pre-existing holes. Indeed, during the HPT processing, the holes were compressed and stretched due to the extensive hydrostatic pressure and torsional deformation. The pre-existing holes' surfaces were brought into contact, stretched and aligned parallel to the normal plane with increasing shear straining. During formation of intimate contact between two internal surfaces large shear strain gradients or even strain discontinuity could develop in the contact region. These strain gradients are known to promote the nucleation of new grains with the orientation very different from that of surrounding matrix [34]. During electro-polishing, the regions of former holes composed of fine grains with high volume fraction of grain boundaries exhibit higher etching rate than the surrounding coarser-grained matrix, thus leading to the formation of the grooves visible in the SE mode of SEM. A closer look in Fig. 4(f, g) confirms the ultrafine size of grains in the groove region. At last, by milling a trench besides a pore located on a groove, several individual pores with widths ranging from 40 to 80 nm were found, Fig. 4(h). These pores were supposed to be residual porosities resulting from relative sliding and incomplete closing of the internal surfaces of the pre-existing holes.

The calculated porosities in the as-cast material, in the HPT-processed Cu disk as well as in the Cu-Holes disk were 0.07 ± 0.01%, 0.07 ± 0.01% and 0.04 ± 0.01%, respectively. Therefore, one can conclude that by introducing pre-existing holes, the generation of percolating porosity near the external surfaces was suppressed. This is probably because the Cu-Holes disk is “softer” than the Cu disk and as a result the slippage and sliding in its the near-surface regions is lower, resulting in fewer pores.

3.2. Microstructure Evolution

In the previous section, SEM-BSE images in Figs. 3 and 4 revealed the co-existence of pores and ultrafine grains within the narrow bands embedded in the matrix of micrometer-sized grains. EBSD measurement was carried out to gain a deeper understanding of the UFGs and porosities evolution.

Fig. 5 shows EBSD maps of two regions in the HPT-processed Cu disk, having pores embedded in UFGs. One map was acquired near (around 20 μm away from) the external surface (Fig. 5a–d), while the other one was taken about 50 μm away from the external surface (Fig. 5e–h). Elongated (Fig. 5a) and nearly round pores (Fig. 5e) were observed in two regions, in agreement with observations in Fig. 3(d, c). By separating the micrometer-sized grains (Fig. 5b, f) and UFGs (Fig. 5c, g), it can be shown that the grain size and crystallography are similar in both regions. The average size of the micrometer-sized grains is about 5 μm, and they contain annealing twins. It should be noted that deformation twinning of ultrapure Cu during the HPT processing is highly improbable, because the stacking fault energy of 5N5 Cu is moderate and large plastic strains can be fully accommodated by dislocation glide

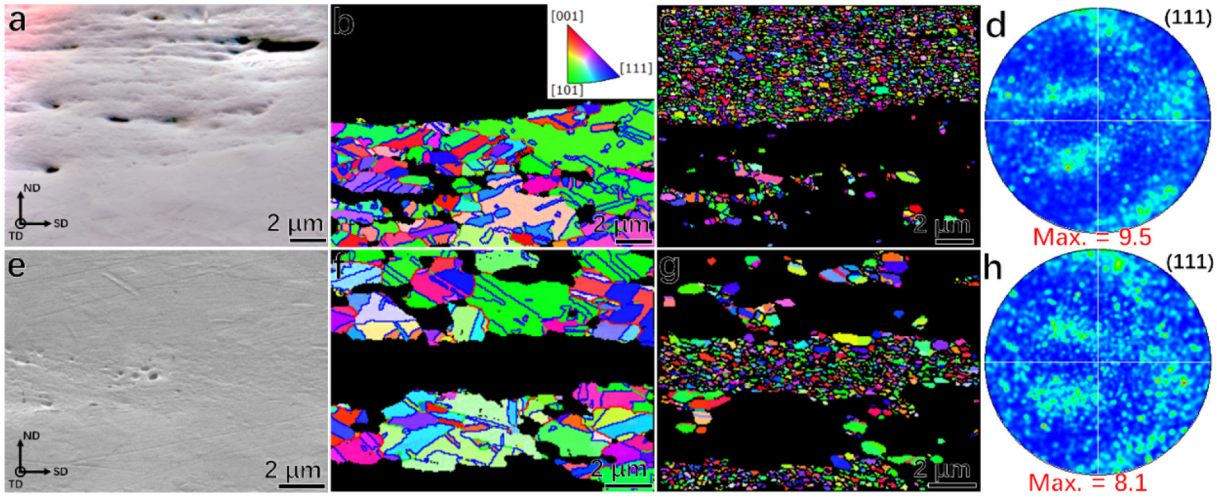

Fig. 5. EBSD measurements of two regions in HPT-processed Cu disk, 20 μm (a–d) and 50 μm (e–h) away from external surface. SEM images showing the topography features of measured area (a, e), orientation images of micrometer-sized grains (b, f), orientation images of UFGs (c, g), and (111) PF of the UFGs (d, h) with maximum intensity labelled. High-angle grain boundaries (HAGBs) and twin boundaries (TBs) are shown in the orientation maps. The legend for orientation maps is shown in (b).

and cross-slip at room temperature [35]. Moreover, the processing was conducted with a moderate strain rate, which is too low for activating the deformation twinning [36]. Therefore, the observed twins can only be annealing twins which could be formed during storage at room temperature and/or sample preparation stage (20 min at 120 °C). The UFGs in the near-surface and more internal regions have average sizes of 323 nm and 458 nm, respectively, and nearly all grain boundaries are high angle grain boundaries (HAGBs). It is worth noting that the average grain size of the UFGs is about the steady-state grain size achievable in 5N5 pure Cu under HPT [37]. The smaller size and narrower size distribution of the UFGs in the region closer to the external surface can be attributed to higher localization of the shear strain due to contact sliding. Finally, by calculating the texture and plotting the (111) pole figures of the UFGs, it can be found that the preferred orientation deviated from simple shear texture due to the shear band slip movement. The bimodal microstructure is clearly not due to abnormal grain growth since the UFG grains were only found in the regions with the induced voids or the vanished pre-existing holes. Therefore, we can conclude that the UFG regions exhibit higher thermal stability and lower grain boundary mobility than the matrix.

The observed pores and UFGs inside of the shear bands were possibly caused by the slippage and sliding between the Cu disk's external surfaces and the anvils [10,38]. It has been found in several studies that dry sliding could cause grain refinement, void nucleation and shear band formation [39–42]. Fig. 6 shows the plausible mechanism for the evolution of porosity and microstructure. At the beginning of the deformation (Fig. 6b), the as-cast coarse grains were refined to submicron size and the as-cast porosity was diminished. Simultaneously, high strain gradients due to the sliding and slippage between the anvils and Cu disk external surfaces result in high strain gradients and accelerated vacancy generation in the near-surface layers. These vacancies agglomerate into clusters and pores and trigger the formation of shear band as a sign of plastic instability, (Fig. 6c). Finally, during the time elapsed between the HPT processing and sample characterization, the recrystallization and twinning occurred in the regions in the matrix but the UFGs inside the shear bands did not coarsen (Fig. 6d). The higher stability of the grains inside the shear bands as compared to those in the matrix can only be explained by vacancy- and pores-induced stabilization mechanisms [43,44]. Due to the extremely low concentration of foreign solutes, less than 0.0005%, the solute drag effect on the GB motion can be neglected. One hypothesis could be that, grains in the shear bands underwent higher extent of lattice rotation than the grains located far from external surfaces [45]. During lattice rotation, excess dislocations and vacancies were annihilated and agglomerated at the grain boundaries. Therefore, higher amount of vacancies was generated for nucleation of pores and concomitant slowing down of grain boundary migration.

The EBSD measurements were conducted on two regions in HPT processed Cu-Holes disk to characterize the groove (pre-existing pore) areas with UFGs. One of the regions exhibit perfect porosity closure and is free of voids in the groove (Fig. 7a–d), the other one has residual voids embedded in the UFGs in the groove (Fig. 7e–h). A comparison of the average grain size and embedded twins inside of the micrometer-sized grains between these two regions did not reveal any significant differences. The average sizes of the UFGs were 539 nm (Fig. 7c) and 511 nm (Fig. 7g). Moreover, the UFGs' preferred orientations aligned very closely to the ideal simple shear orientations [46,47] and they were quite similar as well (seen Fig. 7d, h).

UFGs and simple shear texture were observed in the healed pre-existing hole area. This is believed to be caused by relative sliding between the internal surfaces of the pre-existing holes during HPT. The plausible microstructure evolution is schematically illustrated in Fig. 8. At the beginning of the processing, with the hydrostatic pressure and torsional strain, the pre-existing holes collapsed, and their internal surfaces were stretched (Fig. 8b). With higher straining, the pore was further elongated towards the shearing direction. At the same time, the

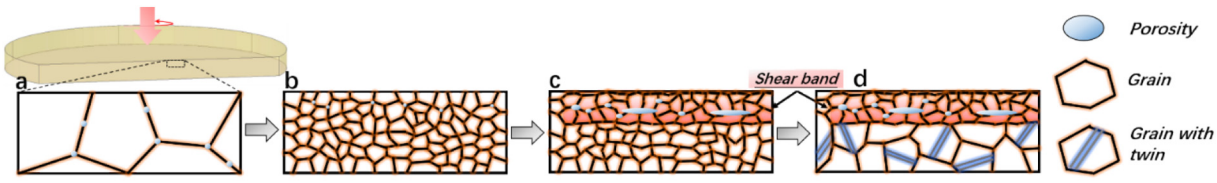

Fig. 6. Schematic illustration of the mechanism of porosity generation and microstructure evolution.

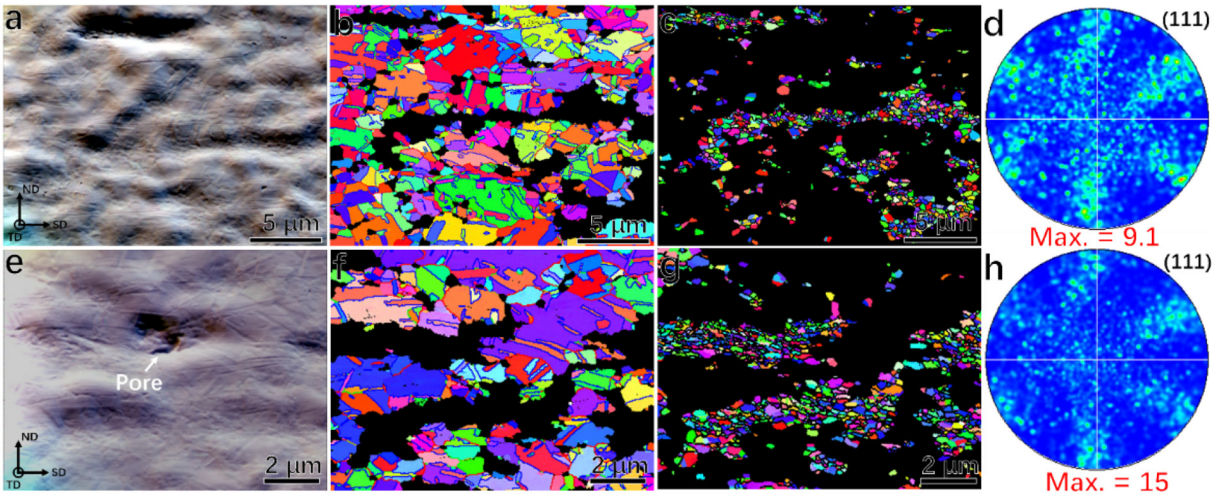

Fig. 7. EBSD measurements of two regions in HPT processed Cu-Holes disk, all pre-existing holes in the region were closed (a–d) and some residual pores existed (e–h). SEM images showing the topography features of measured area (a, e), orientation images of micro-sized grains (b, f), orientation images of UFGs (c, g), and (111) PF of the UFGs (d, h) with maximum intensity labelled. HAGBs and TBs are shown in the orientation maps. Orientation maps use the same legend in Fig. 5.

fragmentation of pore and establishing of intimate atomic contact in some locations between internal surfaces of the hole has occurred (Fig. 8c). In the end, based on the porosity measurement, nearly all internal surfaces were brought into atomic contact and aligned in shear direction, (Fig. 8d). The internal friction between the internal surfaces prior to atomic contact formation has resulted in increased strain gradients and high strain localization, similarly to the situation in the near-surface regions. This, in turn, resulted in increased vacancy production in the regions of pre-existing holes. During the storage at room temperature and/or sample preparation stage, the static recrystallization and twinning occurred in the matrix while the UFGs did not coarsen due to possible vacancy-induced stabilization mechanism (Fig. 8e).

4. Discussion

Most of the studies of porosity generation during plastic deformation were performed employing uniaxial tensile tests of metallic specimens towards ductile failure [48,49]. According to Noell et al.'s recent study [48], excess vacancies would agglomerate and cause nucleation of voids at the cell block boundaries. In this loading condition, extensive UFGs would not form because, without hydrostatic pressure, the formation of voids, shear bands and fractures occur earlier than the rearrangement of dislocation substructures (or fragmentation of microbands).

With increasing stress towards ultimate tensile strength, vacancies are generated from movement of jogged screw dislocations and annihilation of edge dislocations dipoles [48,50,51]. The deformation-induced vacancies, on one hand, will impede the movement of dislocations and contribute to strain hardening; on the other hand, they will induce climb and annihilation of edge dislocations and lead to strain softening [52]. Indeed, the rearrangement of geometrically necessary dislocations (GNDs) to more energy favourable low angle tilt boundaries (LATBs) will require the climb of dislocations to different glide planes [23], for which a high concentration of mobile vacancies is needed. Therefore, one can conclude that, under plastic deformation, vacancies are produced and contribute to the transition of GNDs to LATBs. Under tensile loading with hydrostatic tension component, the rate of vacancy agglomeration at GNDs or dislocation cell block boundaries leading to pores formation is high. In contrast, during SPD processing with hydrostatic compressive pressure, GNDs are able to evolve to LATBs and HAGBs with assistance of vacancy annihilation. Therefore, vacancy diffusion plays a critical role in the generation of porosity.

A number of experimental work using residual electrical resistivity, X-ray line profile analysis, and positron annihilation lifetime spectroscopy have proved that SPD processes such as HPT and ECAP induce high vacancy concentration that is very close to the equilibrium vacancy concentration at the melting point of respective material [52–56]. Here we will assume that the steady-state concentration of vacancies during HPT processing, c_V^{st}, is equal to the equilibrium vacancy concentration at the melting temperature of Cu, $c_V(T_m)$, (T_m = 1358 K):

$$c_V^{st} = c_V(T_m) = g \cdot \exp\left(-\frac{(H_V^M - T_m S_V^M)}{RT_m}\right) \quad (1)$$

where g is a degeneracy factor which means the internal degrees of freedom of point defect [57]. Here $g = 1$ is chosen for monovacancies based on Freysoldt et al.'s work [57]. H_V^F and S_V^F denote the formation enthalpy and formation entropy of a monovacancy, and their values were chosen to be 99.4 kJ mol^{-1} and 1.49 · 10^{-23} J K^{-1}, respectively. It should be noted here that these values were obtained from Neumann et al.'s work [58], and they were tested to be the most accurate ones among other measured values by Andersson and Simak using first-principles approach [59]. With these data, the calculated equilibrium

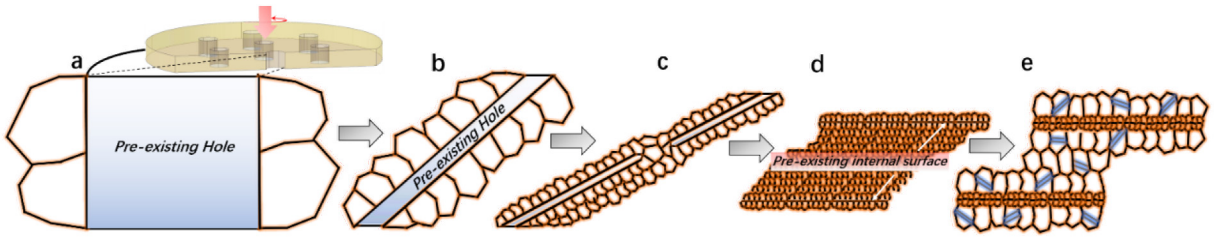

Fig. 8. Schematic illustration of the mechanism of porosity healing and microstructure evolution.

vacancy concentration at the melting point is $c_V(T_m) = 4.43 \cdot 10^{-4}$, which is comparable to the vacancy fraction at melting temperature for pure Cu, $2.1 \cdot 10^{-4}$, from electrical resistivity measurements [60,61], and close to the value, $4.2 \cdot 10^{-4}$, measured from HPT processes pure Cu using differential scanning calorimetry and X-ray Bragg profile analysis [52]. It should be noted that our assumption ${c_V}^{st} = c_V(T_m)$ is based on a reasonable hypothesis that the equilibrium vacancy concentration at the melting point of a metal is a maximum concentration it can sustain [62]. Exceeding this concentration of vacancies leads either to melting or to amorphization.

In addition to intensive vacancy generation during HPT, the diffusivity of vacancies can also be significantly increased by the SPD. Indeed, the systematic studies of several Cu-and Al-based alloys by Straumal et al. [63–69] demonstrated that HPT causes acceleration of mass-transfer and enhancement of diffusivity in excess of what would be expected based on increased vacancy concentration. We will estimate the diffusivity of vacancies during the HPT processing based on a typical size of a pore, $R = 0.1$ μm, achieved after HPT in both samples. The growth of pore during HPT is a result of a competition between the two dynamic processes: absorption of the excess vacancies by the pore leading to its growth, and pore closure caused by shear strain leading to the decrease of its size. We will disregard the latter process which is difficult to treat quantitatively, thus giving the lower bound for the diffusivity of the vacancies. The net vacancy production during HPT, P (the number of vacancies created in the unit volume during 1 s), can be expressed as

$$P = P_0 - Kc_V \tag{2}$$

where P_0 is the net vacancy production due to plastic shear during HPT, and the second term on the right-hand side (RHS) of Eq. (2) describes the rate of vacancies annihilation due to the abundance of internal vacancy sinks (c_V and K being the instant vacancy concentration and the annihilation constant, respectively). The parameters P_0 and K are related: they determine the steady-state vacancy concentration, ${c_V}^{st}$ achievable during HPT: $P_0 = K{c_V}^{st}$. With this relationship in mind, the Eq. (2) can be re-written in the following form:

$$P = K(c_V^{st} - c_V) \tag{3}$$

Once the plastic deformation stops, the constant K determines the kinetics of vacancy concentration relaxation towards its equilibrium value. It can be loosely associated with the reciprocal time needed for the vacancy to reach a nearby sink:

$$K \approx \frac{D_V}{d^2} \tag{4}$$

where D_v and d are the vacancy diffusion coefficient and the distance between the nearest vacancy sinks, respectively. In severely deformed metals the edge dislocations represent the most potent vacancy sinks and sources [70], and keeping the maximum dislocation density achievable during HPT in mind, we will assume $d \approx 50$ nm. Then, the diffusion equation for vacancies taking into account their production by plastic shear and annihilation at the internal sinks and at the surface of the growing pore can be written in the following form:

$$\frac{\partial c_V}{\partial t} = D_v\left(\frac{\partial^2 c_V}{\partial r^2} + \frac{2}{r}\frac{\partial c_V}{\partial r}\right) + K(c_V^0 - c_V) \tag{5}$$

where r is the distance from the center of the growing pore. The Eq. (5) has to be solved with the following boundary conditions:

$$c_V(r = R, t) \approx 0;\ c_V(r \to \infty, t) \approx c_V^{st} \tag{6}$$

For solving the Eq. (5) we will employ the quasi steady-state approximation customary in the theory of phase transformations: $\partial c_V/\partial t \approx 0$. Taking into account the relationship Eq. (4), the Eq. (5) is then transformed into the ordinary differential equation:

$$\frac{d^2 c_V}{dr^2} + \frac{2}{r}\frac{dc_V}{dr} + \frac{c_V^{st} - c_V}{d^2} = 0 \tag{7}$$

With the boundary conditions (6), its solution is

$$c_V = c_V^{st}\left(1 - \frac{R}{r}\exp\left(\frac{R - r}{d}\right)\right) \tag{8}$$

The rate of the pore growth can be determined from the Stefan condition:

$$\frac{dR}{dt} = D_V \frac{dc_V}{dr}\bigg|_{r=R} \tag{9}$$

Substituting the Eqs. (8) into (9) and solving the resulting ordinary differential equation yields the following solution for the pore radius:

$$d(R - R_0) - d^2 \ln\frac{R + d}{R_0 + d} = D_V c_V^{st} t \tag{10}$$

where $R_0 = R(t = 0)$. Assuming $R_0 \ll d$, $R = 100$ nm, $d = 50$ nm, and ${c_V}^{st} = 4.43 \times 10^{-4}$ yields $D_V \approx 1.7 \times 10^{-14}\mathrm{m}^2/\mathrm{s}$ for the vacancies diffusivity during the HPT treatment (at room temperature). It should be emphasized that this value represents the lower bound for vacancy diffusivity, since we neglected the pore closure caused by shear strain. This value has to be compared with the vacancy diffusivity from the extrapolated Arrhenius relationship

$$D_V(T) = D_V^0 \exp\left(-\frac{\Delta H_V^M}{RT}\right) \tag{11}$$

where ${D_V}^0$ denotes the pre-exponential factor and ${\Delta H_V}^M$ is the activation enthalpy of vacancy migration. Their values are $0.13{\cdot}10^{-4}\,\mathrm{m}^2\,\mathrm{s}^{-1}$ and $98.8\,\mathrm{kJ\,mol}^{-1}$, respectively [58]. Due to the small activation volume for vacancy migration we will neglect the contribution of hydrostatic pressure [71]. At room temperature ($T = 300$ K), $D_V(T = 300\mathrm{K}) \approx 8 \times 10^{-23}\mathrm{m}^2/\mathrm{s}$. Thus, the vacancy diffusivity during HPT estimated from the kinetics of pore growth is by more than eight orders of magnitude higher than that estimated from the Arrhenius relationship at room temperature. This increased diffusivity of vacancies is related to the high density of dislocations, since the diffusion along the dislocation core (dislocation pipe diffusion) is several orders of magnitude faster than that in the bulk [72]. Yet the mere pipe diffusion along the static dislocation would not suffice to justify the eight orders of magnitude difference in diffusivities [72]. We believe that during HPT any given vacancy comes into a close proximity of gliding dislocations and/or moving GBs, which may either drag it in the direction of their motion, or provide it with an accelerated diffusion path. Since this process is random in nature and is repeated a number of times, it accelerates the random walk-type movement of the vacancy, which can be formally described by the increased vacancy diffusivity.

5. Conclusions

We have systematically studied the generation and healing of porosity during the HPT processing of ultra-high purity copper. The formation of deformation-induced pores was discussed in terms of increase of vacancy concentration caused by HPT, and accelerated vacancy diffusion. From the result of our study, the following conclusions can be drawn:

1. In the solid Cu disk, the porosity generated by HPT (0.07 ± 0.01 vol%) was close to the initial porosity of the as-cast sample (0.07 ± 0.01%). The major part of the pores was located near the external surfaces of the disk, whereas in the as-cast sample the pores were homogeneously distributed at the grain boundaries through the whole specimen. The pores were embedded in the bands of ultrafine grains of approx. 500 nm in diameter, whereas the pores-free areas of the sample exhibited recrystallized microstructure with coarser grains. We proposed that the observed

porosity was caused by high strain gradients due to relative sliding between anvils and external surfaces, and concomitant accelerated vacancy generation and formation of new ultrafine grains.
2. In the Cu disk with the pre-fabricated holes the porosity decreased from 4.48% to 0.04 ± 0.01% after the HPT processing. Most of the internal surfaces were closed, bonded and embedded in the bands of ultrafine grains with occasional pores. Thus, the "weak" areas of the material associated with the pre-existing holes transformed into the strongest areas of the sample.
3. Ultrafine grains inside of shear bands with pores exhibited higher thermal stability than the surrounding matrix. We attributed this enhanced thermal stability to the drag effect of excess vacancies and pores on the grain boundary motion.
4. We estimated the diffusivity of the vacancies which could lead to pores formation during the HPT processing at room temperature. The obtained diffusivity was by more than eight orders of magnitude higher than the diffusivity extrapolated to room temperature using the Arrhenius relationship obtained at elevated temperatures for the coarse-grain Cu. We attributed the accelerated, "ballistic" movements of the vacancies to the dislocation and grain boundary drag effects.

Acknowledgements

The work was supported by the Ministry of Science & Technology, Israel (grant 3-12418), Ministry of Education and Science of the Russian Federation in the framework of the Program to Increase the Competitiveness of NUST "MISiS", and by Russian Foundation for Basic Research (grant 15-53-06008). YQ would like to thank the support by Technion-Guangdong Postdoctoral Fellowship.

Data Availability

The experimental procedures required to reproduce these findings are available in the "Materials and Methods" section.

References

[1] S. Goods, L. Brown, Overview no. 1: the nucleation of cavities by plastic deformation, Acta Mater. 27 (1979) 1–15.
[2] J.R. Rice, D.M. Tracey, On the ductile enlargement of voids in triaxial stress fields, J. Mech. Phys. Solids. 17 (1969) 201–217.
[3] L. Xue, Damage accumulation and fracture initiation in uncracked ductile solids subject to triaxial loading, Int. J. Solids Struct. 44 (2007) 5163–5181.
[4] S.P. Dudra, Y.T. Im, Analysis of void closure in open-die forging, Int J Mach Tool Manu 30 (1990) 65–75.
[5] M. Nakasaki, I. Takasu, H. Utsunomiya, Application of hydrostatic integration parameter for free-forging and rolling, J. Mater. Process. Technol. 177 (2006) 521–524.
[6] A. Wang, P.F. Thomson, P.D. Hodgson, A study of pore closure and welding in hot rolling process, J. Mater. Process. Technol. 60 (1996) 95–102.
[7] M. Chaaban, J. Alexander, A study of the closure of cavities in swing forging, Proceedings of the Seventeenth International Machine Tool Design and Research Conference, 1997, pp. 633–645.
[8] M. Saby, P.O. Bouchard, M. Bernacki, Void closure criteria for hot metal forming: a review, J. Manuf. Process. 19 (2015) 239–250.
[9] X.X. Zhang, Z.S. Cui, W. Chen, Y. Li, A criterion for void closure in large ingots during hot forging, J. Mater. Process. Technol. 209 (2009) 1950–1959.
[10] T.G. Langdon, Twenty-five years of ultrafine-grained materials: achieving exceptional properties through grain refinement, Acta Mater. 61 (2013) 7035–7059.
[11] Y. Estrin, A. Vinogradov, Extreme grain refinement by severe plastic deformation: a wealth of challenging science, Acta Mater. 61 (2013) 782–817.
[12] C. Haase, R. Lapovok, H.P. Ng, Y. Estrin, Production of Ti–6Al–4V billet through compaction of blended elemental powders by equal-channel angular pressing, Mater. Sci. Eng. A 550 (2012) 263–272.
[13] Y. Qi, K.G. Contreras, H.D. Jung, E.H. Kim, R. Lapovok, Y. Estrin, Ultrafine-grained porous titanium and porous titanium/magnesium composites fabricated by space holder-enabled severe plastic deformation, Mater. Sci. Eng. C 59 (2016) 754–765.
[14] J. Ribbe, D. Baither, G. Schmitz, S.V. Divinski, Network of porosity formed in ultrafine-grained copper produced by equal channel angular pressing, Phys. Rev. Lett. 102 (2009) 165501.
[15] M. Wegner, J. Leuthold, M. Peterlechner, D. Setman, M. Zehetbauer, R. Pippan, S.V. Divinski, G. Wilde, Percolating porosity in ultrafine grained copper processed by high pressure torsion, J. Appl. Phys. 114 (2013) 183509.
[16] S.V. Divinski, G. Wilde, E. Rabkin, Y. Estrin, Ultra-fast atomic transport in severely deformed materials—a pathway to applications? Adv. Eng. Mater. 12 (2010) 779–785.
[17] S.V. Divinski, G. Reglitz, H. Rösner, Y. Estrin, G. Wilde, Ultra-fast diffusion channels in pure Ni severely deformed by equal-channel angular pressing, Acta Mater. 59 (2011) 1974–1985.
[18] J. Ribbe, G. Schmitz, H. Rösner, R. Lapovok, Y. Estrin, G. Wilde, S.V. Divinski, Effect of back pressure during equal-channel angular pressing on deformation-induced porosity in copper, Scr. Mater. 68 (2013) 925–928.
[19] S.V. Divinski, G. Reglitz, I.S. Golovin, M. Peterlechner, R. Lapovok, Y. Estrin, G. Wilde, Effect of heat treatment on diffusion, internal friction, microstructure and mechanical properties of ultra-fine-grained nickel severely deformed by equal-channel angular pressing, Acta Mater. 82 (2015) 11–21.
[20] M. Kawasaki, Different models of hardness evolution in ultrafine-grained materials processed by high-pressure torsion, J. Mater. Sci. 49 (2014) 18–34.
[21] K. Kumagai, T. Sekiguchi, Sharing of secondary electrons by in-lens and out-lens detector in low-voltage scanning electron microscope equipped with immersion lens, Ultramicroscopy 109 (2009) 368–372.
[22] A. Kosinova, B.B. Straumal, A.R. Kilmametov, E. Rabkin, The effect of bismuth on microstructure evolution of ultrafine grained copper, Mater. Lett. 199 (2017) 156–159.
[23] W. Cai, W.D. Nix, Imperfections in Crystalline Solids, Cambridge University Press, 2016.
[24] J. Ribbe, G. Schmitz, Y. Amouyal, Y. Estrin, S.V. Divinski, Grain boundary radiotracer diffusion of Ni in ultra-fine grained Cu and Cu-1wt.% Pb alloy produced by equal channel angular pressing, Mater. Sci. Forum (2008) 380–386. Trans Tech Publ..
[25] S.V. Divinski, J. Ribbe, G. Reglitz, Y. Estrin, G. Wilde, Percolating network of ultrafast transport channels in severely deformed nanocrystalline metals, J. Appl. Phys. 106 (2009) 063502.
[26] R.B. Figueiredo, P.R. Cetlin, T.G. Langdon, Using finite element modeling to examine the flow processes in quasi-constrained high-pressure torsion, Mater. Sci. Eng. A 528 (2011) 8198–8204.
[27] R.B. Figueiredo, M.T.P. Aguilar, P.R. Cetlin, T.G. Langdon, Analysis of plastic flow during high-pressure torsion, J. Mater. Sci. 47 (2012) 7807–7814.
[28] R.B. Figueiredo, G.C.V. de Faria, P.R. Cetlin, T.G. Langdon, Three-dimensional analysis of plastic flow during high-pressure torsion, J. Mater. Sci. 48 (2013) 4524–4532.
[29] S. Panda, L.S. Toth, J.J. Fundenberger, O. Perroud, J. Guyon, J. Zou, T. Grosdidier, Analysis of heterogeneities in strain and microstructure in aluminum alloy and magnesium processed by high-pressure torsion, Mater. Charact. 123 (2017) 159–165.
[30] M. Kamrani, V.I. Levitas, B. Feng, FEM simulation of large deformation of copper in the quasi-constrain high-pressure-torsion setup, Mater. Sci. Eng. A 705 (2017) 219–230.
[31] R.B. Figueiredo, T.G. Langdon, Development of structural heterogeneities in a magnesium alloy processed by high-pressure torsion, Mater. Sci. Eng. A 528 (2011) 4500–4506.
[32] A. Vorhauer, R. Pippan, On the homogeneity of deformation by high pressure torsion, Scr. Mater. 51 (2004) 921–925.
[33] E. Schafler, Strength response upon pressure release after high pressure torsion deformation, Scr. Mater. 64 (2011) 130–132.
[34] F.J. Humphreys, M. Hatherly, Recrystallization and Related Annealing Phenomena, Elsevier, 2012.
[35] V.S. Sarma, J. Wang, W.W. Jian, A. Kauffmann, H. Conrad, J. Freudenberger, Y.T. Zhu, Role of stacking fault energy in strengthening due to cryo-deformation of FCC metals, Mater. Sci. Eng. A 527 (2010) 7624–7630.
[36] C.X. Huang, K. Wang, S.D. Wu, Z.F. Zhang, G.Y. Li, S.X. Li, Deformation twinning in polycrystalline copper at room temperature and low strain rate, Acta Mater. 54 (2006) 655–665.
[37] K. Edalati, Z. Horita, High-pressure torsion of pure metals: influence of atomic bond parameters and stacking fault energy on grain size and correlation with hardness, Acta Mater. 59 (2011) 6831–6836.
[38] K. Edalati, Z. Horita, T.G. Langdon, The significance of slippage in processing by high-pressure torsion, Scr. Mater. 60 (2009) 9–12.
[39] A. Emge, S. Karthikeyan, D. Rigney, The effects of sliding velocity and sliding time on nanocrystalline tribolayer development and properties in copper, Wear 267 (2009) 562–567.
[40] H.C. How, T.N. Baker, Characterisation of sliding friction-induced subsurface deformation of Saffil-reinforced AA6061 composites, Wear 232 (1999) 106–115.
[41] X. Wei, M. Hua, Z. Xue, Z. Gao, J. Li, Evolution of friction-induced microstructure of SUS 304 meta-stable austenitic stainless steel and its influence on wear behavior, Wear 267 (2009) 1386–1392.
[42] L. Meshi, S. Samuha, S.R. Cohen, A. Laikhtman, A. Moshkovich, V. Perfilyev, I. Lapsker, L. Rapoport, Dislocation structure and hardness of surface layers under friction of copper in different lubricant conditions, Acta Mater. 59 (2011) 342–348.
[43] Y. Estrin, K. Lücke, Theory of vacancy-controlled grain boundary motion, Acta Mater. 30 (1982) 983–998.
[44] L. Klinger, E. Rabkin, L.S. Shvindlerman, G. Gottstein, Grain growth in porous two-dimensional nanocrystalline materials, J. Mater. Sci. 43 (2008) 5068–5075.
[45] J. Sun, P. Trimby, F. Yan, X. Liao, N. Tao, J. Wang, Shear banding in commercial pure titanium deformed by dynamic compression, Acta Mater. 79 (2014) 47–58.
[46] S. Li, I.J. Beyerlein, M.A. Bourke, Texture formation during equal channel angular extrusion of fcc and bcc materials: comparison with simple shear, Mater. Sci. Eng. A 394 (2005) 66–77.
[47] S.R. Kalidindi, C.A. Bronkhorst, L. Anand, Crystallographic texture evolution in

bulk deformation processing of FCC metals, J. Mech. Phys. Solids. 40 (1992) 537–569.
[48] P. Noell, J. Carroll, K. Hattar, B. Clark, B. Boyce, Do voids nucleate at grain boundaries during ductile rupture? Acta Mater. 137 (2017) 103–114.
[49] G. Gerstein, H.B. Besserer, F. Nürnberger, L.A. Barrales-Mora, L.S. Shvindlerman, Y. Estrin, H.J. Maier, Formation and growth of voids in dual-phase steel at micro-scale and nanoscale levels, J. Mater. Sci. 52 (2017) 4234–4243.
[50] G.E. Dieter, D.J. Bacon, Mechanical Metallurgy, McGraw-Hill, New York, 1986.
[51] U. Essmann, H. Mughrabi, Annihilation of dislocations during tensile and cyclic deformation and limits of dislocation densities, Philos. Mag. A. 40 (1979) 731–756.
[52] M.J. Zehetbauer, G. Steiner, E. Schafler, A.V. Korznikov, E. Korznikova, Deformation induced vacancies With severe plastic deformation: Measurements and modelling, Mater. Sci. Forum (2006) 57–64. Trans Tech Publ..
[53] A.R. Kilmametov, G. Vaughan, A. Yavari, A. LeMoulec, W. Botta, R. Valiev, Microstructure evolution in copper under severe plastic deformation detected by in situ X-ray diffraction using monochromatic synchrotron light, Mater. Sci. Eng. A 503 (2009) 10–13.
[54] J. Čížek, M. Janeček, O. Srba, R. Kužel, Z. Barnovská, I. Procházka, S. Dobatkin, Evolution of defects in copper deformed by high-pressure torsion, Acta Mater. 59 (2011) 2322–2329.
[55] D. Setman, E. Schafler, E. Korznikova, M.J. Zehetbauer, The presence and nature of vacancy type defects in nanometals detained by severe plastic deformation, Mater. Sci. Eng. A 493 (2008) 116–122.
[56] L.H. Su, C. Lu, L.Z. He, L.C. Zhang, P. Guagliardo, A.K. Tieu, S.N. Samarin, J.F. Williams, H.J. Li, Study of vacancy-type defects by positron annihilation in ultrafine-grained aluminum severely deformed at room and cryogenic temperatures, Acta Mater. 60 (2012) 4218–4228.
[57] C. Freysoldt, B. Grabowski, T. Hickel, J. Neugebauer, G. Kresse, A. Janotti, C.G. Van de Walle, First-principles calculations for point defects in solids, Rev. Mod. Phys. 86 (2014) 253.
[58] G. Neumann, V. Tölle, C. Tuijn, Monovacancies and divacancies in copper: re-analysis of experimental data, Phys. B Condens. Matter 271 (1999) 21–27.
[59] D.A. Andersson, S. Simak, Monovacancy and divacancy formation and migration in copper: a first-principles theory, Phys. Rev. B 70 (2004) 115108.
[60] H.J. Wollenberger, Physical Metallurgy (Fourth, Revised and Enhanced Edition) (North-Holland, Oxford), (1996).
[61] P. Wright, J. Evans, Formation and migration energies of vacancies in copper, Philos. Mag. 13 (1966) 521–531.
[62] R.W. Cahn, Crystal defects and melting, Nature 273 (1978) 491–492.
[63] B.B. Straumal, S.G. Protasova, A.A.A. Mazilkin, E. Rabkin, D. Goll, G. Schütz, B. Baretzky, R.Z. Valiev, Deformation-driven formation of equilibrium phases in the Cu–Ni alloys, J. Mater. Sci. 47 (2012) 360–367.
[64] B.B. Straumal, A.R. Kilmametov, Y. Ivanisenko, L. Kurmanaeva, B. Baretzky, Y.O. Kucheev, P. Zięba, A. Korneva, D.A. Molodov, Phase transitions during high pressure torsion of Cu–Co alloys, Mater. Lett. 118 (2014) 111–114.
[65] B.B. Straumal, A.A.A. Mazilkin, B. Baretzky, G. Schütz, E. Rabkin, R.Z. Valiev, Accelerated diffusion and phase transformations in Co–Cu alloys driven by the severe plastic deformation, Mater. Trans. 53 (2012) 63–71.
[66] A. Korneva, B.B. Straumal, A.R. Kilmametov, R. Chulist, P. Straumal, P. Zięba, Phase transformations in a Cu–Cr alloy induced by high pressure torsion, Mater. Charact. 114 (2016) 151–156.
[67] B.B. Straumal, V. Pontikis, A.R. Kilmametov, A.A. Mazilkin, S. Dobatkin, B. Baretzky, Competition between precipitation and dissolution in Cu–Ag alloys under high pressure torsion, Acta Mater. 122 (2017) 60–71.
[68] B.B. Straumal, A.R. Kilmametov, G. López, I. López-Ferreño, M. Nó, J. San Juan, H. Hahn, B. Baretzky, High-pressure torsion driven phase transformations in Cu–Al–Ni shape memory alloys, Acta Mater. 125 (2017) 274–285.
[69] B.B. Straumal, X. Sauvage, B. Baretzky, A.A. Mazilkin, R. Valiev, Grain boundary films in Al–Zn alloys after high pressure torsion, Scr. Mater. 70 (2014) 59–62.
[70] D.N. Seidman, R.W. Balluffi, Sources of thermally-generated vacancies in single-crystal and polycrystalline gold, Phys. Rev. 139 (A) (1965) 1824–1840.
[71] J.M. Philibert, Atom Movements-diffusion and Mass Transport in Solids, EDP Sciences, 2012.
[72] I. Kaur, Y. Mishin, W. Gust, Fundamentals of Grain and Interphase Boundary Diffusion, 3rd edition, Wiley and Sons, Chichester, 1995.